Evaporation-Driven Cellular Patterns in Confined Hyperelastic Hydrogels

Baudouin Saintyves,[1,2,*] Romain Pic,[1] L. Mahadevan,[3] and Irmgard Bischofberger[1,†]
[1]Department of Mechanical Engineering, Massachusetts Institute of Technology, Cambridge, Massachusetts 02139, USA
[2]James Franck Institute and Department of Physics, The University of Chicago, Chicago, Illinois 60637, USA
[3]John A. Paulson School of Engineering and Applied Sciences, Department of Physics, Department of Organismic and Evolutionary Biology, Harvard University, Cambridge, Massachusetts 02138, USA

(Received 30 April 2023; accepted 8 August 2023; published 15 September 2023)

When a hyperelastic hydrogel confined between two parallel glass plates begins to dry from a lateral boundary, the volume lost by evaporation is accommodated by an inward displacement of the air-hydrogel interface that induces an elastic deformation of the hydrogel. Once a critical front displacement is reached, we observe intermittent fracture events initiated by a geometric instability resulting in localized bursts at the interface. These bursts relax the stresses and irreversibly form air cavities that lead to cellular networks. We show that the spatial extent of the strain field prior to a burst, influenced by the air-hydrogel interfacial tension and the confinement of the gel, determines the characteristic size of the cavities.

DOI: 10.1103/PhysRevLett.131.118202

Cracks in paintings and colloidal suspensions [1,2], buckling of pollen grains [3], and columnar joint formation in rocks [4] are examples where multiphase solids develop patterns as the solvent evaporates. The interplay between drying-induced shrinkage gradients in the material and geometric constraints induces mechanical stresses that lead to structural deformation and failure [5–7]. In evaporating sessile drops and films of colloidal suspensions, intricate fracture patterns form in the dried close-packed particle deposit, characterized by brittle cracks that are governed by the release of flow-induced tensile stresses [8–11]. In polymer gels, where the solvent concentration is typically higher, evaporation can induce large shrinkage before the material reaches an arrested glassy state [5]. This affects the resulting morphologies; during the drying of a cylindrical piece of gel, for example, the deformation is not sufficient to induce patterns, unless a glassy crust forms on the softer inner gel and wrinkles develop [12]. However, under strong geometrical constraints, such as in confinement, larger elastic deformations might emerge. In highly stretchable materials subjected to fluid injection or tensile tests, instabilities and material failure resulting from nonlinear mechanics at large deformations have been reported [13–20]. Here we probe the regime where nonlinear deformations are induced by solvent evaporation.

We report a unique type of cellular pattern growth that emerges in highly deformable hydrogels confined between two parallel plates [Fig. 1(a)]; upon drying, air cavities intermittently burst into the hydrogel creating a cellular network of cavities, as shown in Fig. 1(b). The temporal evolution of the interface reveals two regimes of growth: a slow expansion of a cavity to a critical front displacement followed by an irreversible fracture that leads to the formation of a new cavity. Following such an event, the surrounding air-hydrogel interface recedes indicating a relaxation of elastic stresses as a new cavity emerges. The characteristic size of the cavities increases with increasing spacing between the two plates and decreases

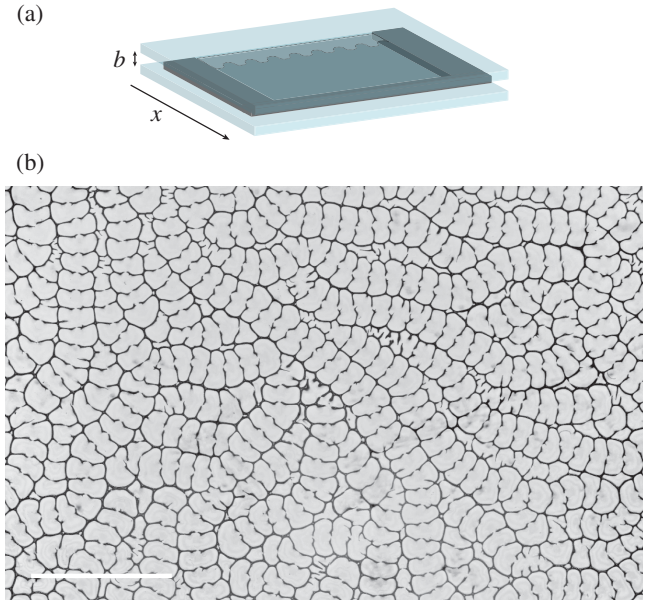

FIG. 1. (a) Schematic of the experimental setup. A polyacrylamide hydrogel is confined between two parallel plates separated by a spacing b. Three sides of the cell are closed and water evaporates from the side open to atmosphere, in the x direction. (b) Cellular patterns appear due to the differential drying induced by evaporation, progressing from the top and moving downwards. The hydrogel has a modulus $G = 80$ Pa, the plate spacing is $b = 25$ μm. The scale bar denotes 2 mm.

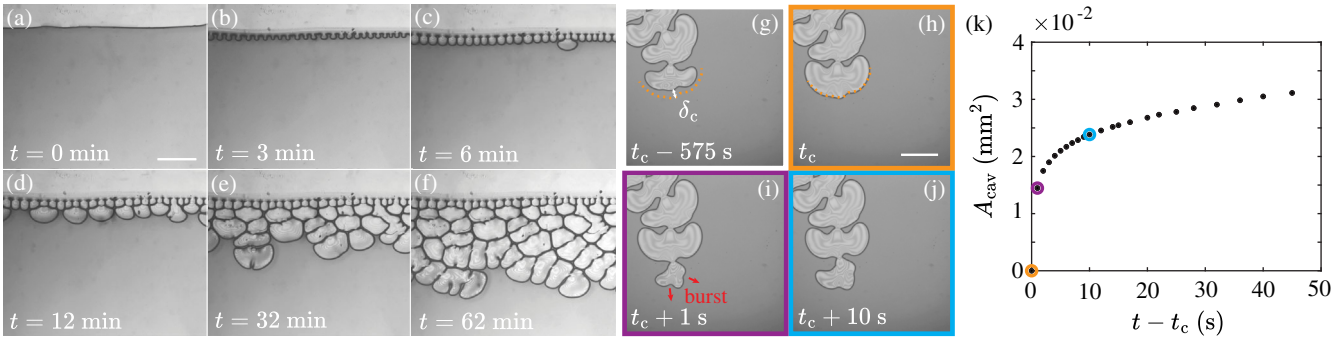

FIG. 2. (a)–(f) Temporal evolution of the pattern growth for a hydrogel with modulus $G = 80$ Pa and a plate spacing $b = 25$ μm (Movie S1 [22]). The scale bar denotes 500 μm. (a),(b) The initially flat air-hydrogel interface advances inwards and destabilizes via an elastic instability into regularly spaced fingers. (c),(d) A first set of cavities burst at the interface. (e),(f) More cavities emerge and invade the cell. (g)–(k) Snapshots of the emergence of a new cavity at $t = t_c$, and corresponding temporal evolution of the cavity area A_{cav} (Movie S2 [22]). The hydrogel modulus is $G = 15$ Pa and the plate spacing is $b = 15$ μm. The scale bar denotes 200 μm. Before t_c (g), (h), the cavity front grows at a rate set by evaporation to a critical front displacement δ_c. At t_c, a new cavity bursts (i) leading to a rapid increase of A_{cav}. (j) The burst arrests and the growth recovers the regime of slow front displacement. (k) Temporal evolution of the cavity area A_{cav}.

weakly with the hydrogel modulus. We rationalize this selection of cavity size in a scaling model that accounts for the elastic strain stored in the deformed hydrogel, which are affected by the interfacial tension at the air-hydrogel interface.

Drying experiments are performed in cells made of two microscope glass plates of length 25 mm, width 25 mm and thickness 1 mm. The spacing between the plates ranges from $b = 5$–250 μm controlled by calibrated spacers (Precision Brand) or by UV-polymerized SU-8 photoresist (MicroChem). The cells are sealed on three sides to induce evaporation from the one open side only. The adhesion between the hydrogel and the cell is ensured by coating the glass plates with acrylate brushes (Sigma-Aldrich) [21]. Drying takes place in a closed transparent container at temperatures of $T = 23\,°C$ or $T = 50\,°C$, and at relative humidity $< 10\%$. The final drying pattern is unaffected by temperature in this range. The patterns are imaged on an inverted microscope (Eclipse TE2000-U, Nikon) equipped with a digital camera (Lumix GH5) or a high-speed camera (Photron). Data are extracted from photographs of the final dried samples, or from time-lapse images recorded at frame rates of 0.5, 1, or 400 frames/ sec.

The hydrogels are composed of polyacrylamide at concentrations ranging from 3–8 wt%. Acrylamide monomers (Bio-Rad Laboratories), the crosslinker bis-acrylamide (Bio-Rad Laboratories), the initiator potassium persulfate (Sigma-Aldrich) and the catalyst tetramethyldiamine (Sigma-Aldrich) are mixed in deionized water [22]. The solution is filled into the cell in the liquid state by capillary action or injection. Gelation occurs in a water-saturated desiccator for two hours. The hydrogels have storage moduli ranging between $G' \equiv G = 11$–2200 Pa, as measured in the linear elastic regime using a stress-controlled rheometer (AR-G2, TA Instruments). The hydrogels are highly deformable and exhibit failure strains $> 100\%$ [22].

At the end of the drying process, the hydrogels exhibit morphologies that are distinct from those observed in confined close-packed colloidal deposits, where drying induces straight cracks [2,23–25]. Instead, we observe a network of air cavities separated by thin walls composed of dried hydrogel and connected through small air openings, as shown in Fig. 1(b). The cavities form in the bulk of the hydrogel, as evidenced by the existence of dried gel on both glass plates observed upon opening the cell.

We follow the growth of the air cavities via time-lapse imaging under an optical microscope. In a first stage, the flat air-hydrogel interface advances inward as water evaporates. The interface eventually destabilizes into regularly spaced air fingers [Figs. 2(a),2(b)]. These fingers are similar to those observed as confined hydrogels are deformed via fluid injection or in debonding experiments, and are the result of a reversible elastic instability [15–17]. In a second stage, larger cavities appear through localized and intermittent bursts at the destabilized interface, which invade the entire hydrogel, as shown in Figs. 2(c)–2(f). The bursts are irreversible events that locally fracture the hydrogel. Focusing on a single cavity, the interface first grows slowly, expanding radially by a displacement δ [Fig. 2(g)]. When a critical value δ_c is reached [Fig. 2(h)], a new cavity emerges by a rapid irreversible growth [Figs. 2(i)–2(k)]. The process is then repeated as the drying front progresses through the system.

As water evaporates from the hydrogel, the hydrophilic gel initially deforms elastically while losing water from within the matrix. This leads to a buildup of elastic stress, primarily in the vicinity of the air-hydrogel interface [5] where water loss is largest. The poroelastic deformation of the polymer matrix driven by water flow has an associated timescale given by $\tau_p = (\eta b \delta)/(G\xi^2)$, where η is the water viscosity, δ the front displacement, and ξ the hydrogel pore size [26]. We evaluate the importance of poroelastic

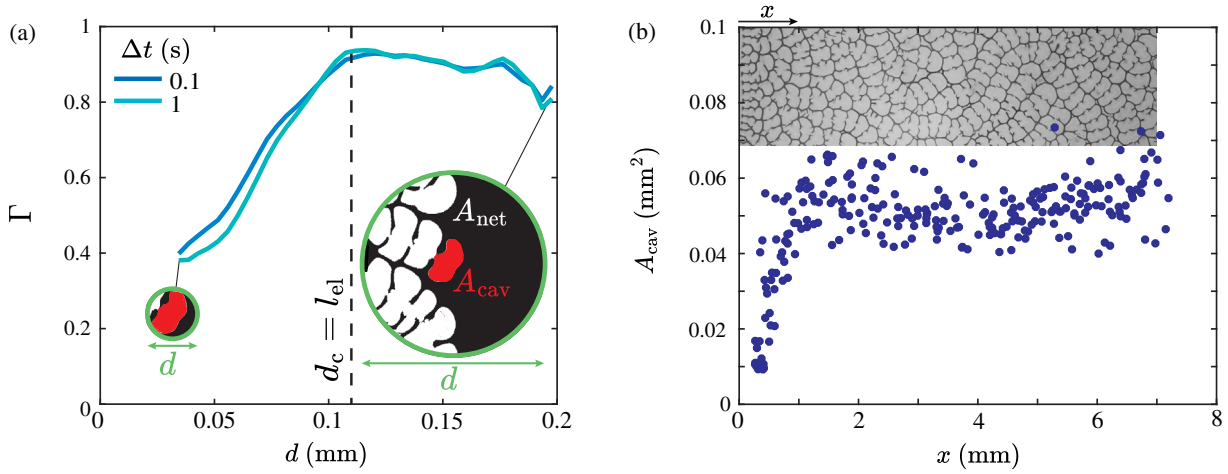

FIG. 3. (a) Area conservation during the burst of a single cavity expressed by $\Gamma(\Delta t) = [A_{\mathrm{net}}(\Delta t = 0) - A_{\mathrm{net}}(\Delta t)]/A_{\mathrm{cav}}(\Delta t)$ measured in circular regions of diameters d around the cavity center, for different Δt and for a hydrogel with $G = 80$ Pa and $b = 25$ μm. The images show binarized masks used to determine the area of the network of cavities A_{net} (white) and the area of a new cavity A_{cav} (red). (b) Area of cavities A_{cav} versus the distance x from the initial air-hydrogel interface for a hydrogel with $G = 134$ Pa and $b = 25$ μm.

effects by comparing τ_{p} with the characteristic loading time $\tau_{\mathrm{e}} = \delta/\dot{r}$, where $\dot{r}$ is related to the air-hydrogel interface velocity [22]. This yields $\tau_{\mathrm{p}}/\tau_{\mathrm{e}} = \eta b\dot{r}/(G\xi^2)$. Using representative values of $\xi \sim 100$ nm [27] and $\dot{r} \sim 10^{-7}$ m/s, we find $\tau_{\mathrm{p}}/\tau_e \sim 10^{-4}$–$10^{-1}$ for the range of G and b investigated [22]. Poroelastic effects are thus negligible during the slowly moving phase of the drying front.

To probe the relaxation of the air-hydrogel interface that occurs upon a burst, we define the area of the network of cavities that are formed at time Δt as $A_{\mathrm{net}}(\Delta t)$ and the area of the new cavity at time Δt as $A_{\mathrm{cav}}(\Delta t)$. The area ratio $\Gamma(\Delta t) = (A_{\mathrm{net}}(\Delta t = 0) - A_{\mathrm{net}}(\Delta t))/A_{\mathrm{cav}}(\Delta t)$ then corresponds to the ratio of the newly lost network area from the relaxing air-hydrogel interface and the area gained from the newly formed cavity. To quantify the spatial extent of the interface relaxation, we measure $\Gamma(\Delta t)$ within circular masks of diameter d centered on the new cavity, as shown in Fig. 3(a) for $\Delta t = 0.1$ and $\Delta t = 1$ s. We find that Γ increases with increasing mask diameter and reaches a plateau value $\Gamma \sim 0.9$ at a critical mask diameter d_{c} that characterizes the spatial extent l_{el} of the stress field at the onset of a burst. This almost complete area conservation indicates that a burst induces a simple elastic relaxation of the hydrogel matrix via cavity formation.

To characterize the cavity size, we analyze photographs of fully dried samples and find that the cavity area A_{cav} increases monotonically from the initial front location at $x = 0$ and reaches a constant value $A_{\mathrm{cav}}^{\infty}$ in the interior of the cell, as shown in Fig. 3(b) for a hydrogel with $G = 80$ Pa and $b = 25$ μm. We define an average cavity size in the plateau regime as $L_{\mathrm{cav}} = (1/N)\sum_{i=1}^{N}\sqrt{A_{\mathrm{cav},i}^{\infty}}$, where N is the total number of cavities, and find that L_{cav} increases with increasing plate spacing and decreases weakly with the hydrogel modulus, as shown in Figs. 4(a),4(b). The critical front displacement at burst δ_c, by contrast, is independent of G and increases linearly with b, as shown in the inset of Fig. 4(b). This rules out that the sudden burst at the end of the slow growth regime is triggered as the front displacement reaches the failure strain of the hydrogel measured in rheology, as this failure strain exhibits a strong dependence on G [22].

The independence of the burst strain δ_c/b on the hydrogel modulus suggests a triggering mechanism that is purely geometric. This is reminiscent of a reversible elastic instability of geometric origin observed as air is injected into bulk polyacrylamide hydrogels [15]. Such instability can trigger an irreversible fracture that propagates across the material [14]. Instead, in the present case of evaporation-driven loading under confinement, we observe multiple arrested fractures that lead to cavities of well-defined length scale. To rationalize this distinct phenomenology, we consider (i) that the elastic instability occurs as the air-hydrogel interface reaches a critical front displacement $\delta_c \sim b$, (ii) that this instability triggers a fracture, and (iii) that the area of gel lost upon a cavity burst is recovered in the vicinity of the burst, as sketched in Fig. 4(c). During slow cavity growth, the strain grows to a value that scales as $(\gamma/bG) + f(\delta)$, since the interfacial pressure jump scales as γ/b, where γ is the air-hydrogel interfacial tension and $f(\delta)$ the elastic deformation from the evaporation [28].

For $\gamma/bG \ll 1$ where interfacial tension effects are negligible, the drying in the slow growth regime is accompanied by the buildup of a strain field of spatial extent l_{el} that is set by the smaller of the geometric length scales given by the plate spacing, $l_{\mathrm{el}} \sim b$ [16]. In this

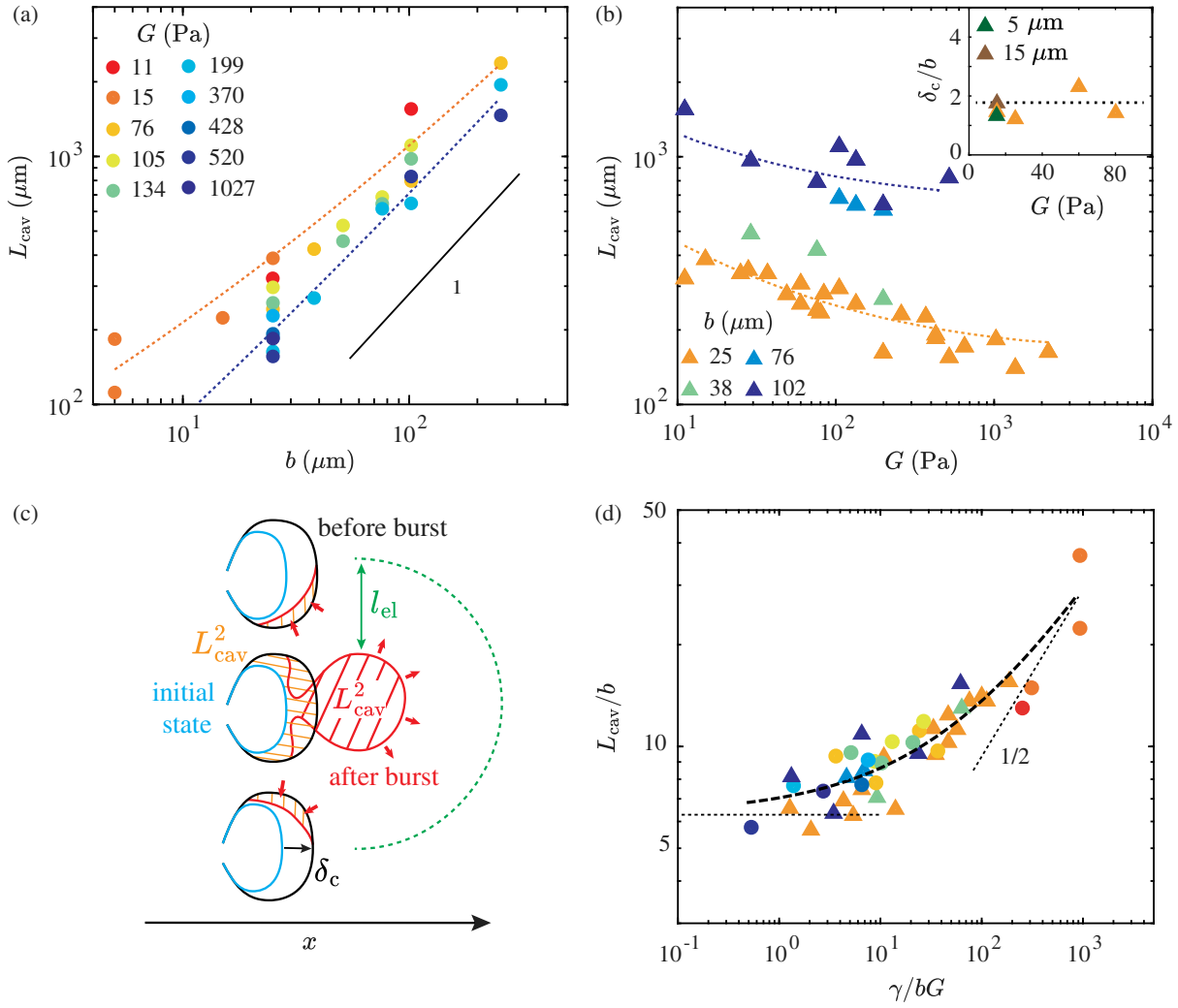

FIG. 4. (a) Cavity size L_{cav} versus the plate spacing b for hydrogels with moduli ranging from $G = 11$–1027 Pa. (b) Cavity size L_{cav} versus the modulus G for plate spacings ranging from $b = 25$–102 μm. Inset: Normalized critical front displacement at burst δ_c/b as a function of the modulus G, obtained from time-lapse images of selected samples. The dotted lines in (a) and (b) correspond to Eq. (1), with fit parameters determined from the master curve in (d) and with $G = 76$ Pa (orange) and 520 Pa (blue) in (a), and $b = 25$ μm (orange) and 102 μm (blue) in (b). (c) Top view schematic of a burst. x denotes the direction of front propagation. Because of area conservation, the area of a new cavity [$\sim L^2_{cav}$ (red)] is equal to the network area lost upon the burst occurring as $\delta = \delta_c$ (orange) within a region of size l_{el} (green dotted line). This yields $L^2_{cav} \sim l_{el}\delta_c$. (d) Master curve of the normalized cavity size L_{cav}/b versus the dimensionless parameter γ/bG. For $\gamma/bG \ll 1$, the cavity size is dominated by the gel elasticity where $L_{cav} \sim b$. For $\gamma/bG \gg 1$, the cavity size is governed by elastocapillary effects, where $L_{cav}/b \sim \sqrt{\gamma/(bG)}$. The dashed line denotes $L_{cav}/b = 6.3 + 0.7\sqrt{\gamma/(bG)}$.

regime, the interface curvature evolves to optimize the elastic energy stored in the matrix. For $\gamma/bG \gg 1$, the high cost for creating new interface results in a smaller curvature than that adopted if interfacial tension effects are negligible, which induces a larger strain close to the two plates. This larger strain at the plates is accommodated by a larger spatial extent of the strain field into the hydrogel, which we hypothesize to be set by the elastocapillary length scale $l_{el} \sim \gamma/G$ in this regime [29].

The formation of a cavity relaxes the stresses over the length scale l_{el}, which together with the area conservation upon a burst when $\delta = \delta_c$ suggests that $L^2_{cav} \sim l_{el}\delta_c$. We then expect $L_{cav}/b \sim 1$ in the elasticity dominated regime and $L_{cav}/b \sim \sqrt{\gamma/(bG)}$ in the interfacial tension dominated one. In a crossover regime where both effects are of comparable magnitude, we expect a larger spatial extent of the strain field than in the purely elastic case. In general, we postulate the normalized cavity size to scale as

$$\frac{L_{cav}}{b} \sim 1 + \sqrt{\frac{\gamma}{bG}}, \tag{1}$$

which is in good agreement with our experimental data, as shown in Fig. 4(d) where we report L_{cav}/b versus γ/bG, and find that a fit to Eq. (1) yields prefactors of order 1.

In summary, we show how the evaporation of a confined hydrogel induces the irreversible growth of cellular patterns of air cavities with well-defined characteristic size. The burst of a new cavity occurs at a critical front displacement that is independent of the hydrogel modulus and set by the geometric confinement. We rationalize the size of the cavities by considering the elastic strain stored in the material at the onset of a burst whose spatial range can be affected by interfacial tension effects. Our work paves the way for theoretical work on drying-induced instabilities in strongly deformable materials. For example, the neo-Hookean framework developed in [16,17,29] might be expanded to include an elastic energy density function that considers a strain induced by material loss from evaporation, as well as irreversible effects due to damage and failure. Along another axis, our work shows that complex structures and specific length scales can be "encoded" within the material through mechanical constraints. Going beyond the evaporation protocols commonly used in the industrial production of homogeneous films, this could open new avenues for fabrication, for example, by designing topographic constraints induced by spatially variable confinement and moduli, or by utilizing nematic gels.

We thank Severine Atis, François Boulogne, Alfred Crosby, and Thomas Witten for helpful discussions. B. S. and I. B. acknowledge support from the MIT Research Support Committee. L. M. thanks the Harvard MRSEC 2011754, the Simons Foundation and the Henri Seydoux Fund for partial financial support.

*saintyves@uchicago.edu
†irmgard@mit.edu

[1] F. Giorgiutti-Dauphiné and L. Pauchard, J. Appl. Phys. **120**, 065107 (2016).
[2] E. R. Dufresne, D. J. Stark, N. A. Greenblatt, J. X. Cheng, J. W. Hutchinson, L. Mahadevan, and D. A. Weitz, Langmuir **22**, 7144 (2006).
[3] E. Katifori, S. Alben, E. Cerda, D. R. Nelson, and J. Dumais, Proc. Natl. Acad. Sci. U.S.A. **107**, 7635 (2010).
[4] L. Goehring, L. Mahadevan, and S. W. Morris, Proc. Natl. Acad. Sci. U.S.A. **106**, 387 (2009).
[5] C. J. Brinker and G. W. Scherer, *Sol-Gel Science: The Physics and Chemistry of Sol-Gel Processing* (Elsevier, London, 1990).
[6] E. Reyssat and L. Mahadevan, J. R. Soc. Interface **6**, 951 (2009).
[7] F. Boulogne and H. A. Stone, Europhys. Lett. **108**, 19001 (2014).
[8] L. Goehring, W. J. Clegg, and A. F. Routh, Phys. Rev. Lett. **110**, 024301 (2013).
[9] A. F. Routh, Rep. Prog. Phys. **76**, 046603 (2013).
[10] P. Lilin and I. Bischofberger, Langmuir **38**, 7442 (2022).
[11] P. Bourrianne, P. Lilin, G. Sintès, T. Nîrca, G. H. McKinley, and I. Bischofberger, Soft Matter **17**, 8832 (2021).
[12] K. Huraux, T. Narita, B. Bresson, C. Frétigny, and F. Lequeux, Soft Matter **8**, 8075 (2012).
[13] A. N. Gent, Int. J. Nonlinear Mech. **40**, 165 (2005).
[14] S. Kundu and A. J. Crosby, Soft Matter **5**, 3963 (2009).
[15] B. Saintyves, O. Dauchot, and E. Bouchaud, Phys. Rev. Lett. **111**, 047801 (2013).
[16] J. S. Biggins, B. Saintyves, Z. Wei, E. Bouchaud, and L. Mahadevan, Proc. Natl. Acad. Sci. U.S.A. **110**, 12545 (2013).
[17] J. S. Biggins, Z. Wei, and L. Mahadevan, Europhys. Lett. **110**, 34001 (2015).
[18] C. W. Barney, C. E. Dougan, K. R. McLeod, A. Kazemi-Moridani, Y. Zheng, Z. Ye, S. Tiwari, I. Sacligil, R. A. Riggleman, S. Cai, J.-H. Lee, S. R. Peyton, G. N. Tew, and A. J. Crosby, Proc. Natl. Acad. Sci. U.S.A. **117**, 9157 (2020).
[19] S. B. Hutchens, S. Fakhouri, and A. J. Crosby, Soft Matter **12**, 2557 (2016).
[20] A. Delbos, J. Cui, S. Fakhouri, and A. J. Crosby, Soft Matter **8**, 8204 (2012).
[21] H. Yuk, T. Zhang, S. Lin, G. A. Parada, and X. Zhao, Nat. Mater. **15**, 190 (2015).
[22] See Supplemental Material at http://link.aps.org/supplemental/10.1103/PhysRevLett.131.118202 for Figs. S1 and S2, and for the preparation protocol and the characterization of the hydrogels.
[23] C. Allain and L. Limat, Phys. Rev. Lett. **74**, 2981 (1995).
[24] E. R. Dufresne, E. I. Corwin, N. A. Greenblatt, J. Ashmore, D. Y. Wang, A. D. Dinsmore, J. X. Cheng, X. S. Xie, J. W. Hutchinson, and D. A. Weitz, Phys. Rev. Lett. **91**, 224501 (2003).
[25] F. Boulogne, L. Pauchard, F. Giorgiutti-Dauphiné, R. Botet, R. Schweins, M. Sztucki, J. Li, B. Cabane, and L. Goehring, Europhys. Lett. **105**, 38005 (2014).
[26] E. Moeendarbary, L. Valon, M. Fritzsche, A. R. Harris, D. A. Moulding, A. J. Thrasher, E. Stride, L. Mahadevan, and G. T. Charras, Nat. Mater. **12**, 253 (2013).
[27] D. L. Holmes and N. C. Stellwagen, Electrophoresis **12**, 612 (1991).
[28] K. R. Shull and C. Creton, J. Polym. Sci. Part B **42**, 4023 (2004).
[29] J. S. Biggins and L. Mahadevan, Soft Matter **14**, 7680 (2018).